Aerospace Science and Technology 168 (2026) 110846

Contents lists available at ScienceDirect

Aerospace Science and Technology

journal homepage: www.elsevier.com/locate/aescte

Original article

Breakdown of boundary layer instabilities on a straight cone in a hypersonic shock tunnel

Divek Surujhlal *, Alexander Wagner, Marco Costantini, Massimo Miozzi

German Aerospace Centre DLR, Göttingen, Germany

ARTICLE INFO

Communicated by Cummings Russell

Keywords:
Boundary layer transition
Hypersonics
Instabilities
Shock tunnel

ABSTRACT

Experimental investigations of the second-mode dominated hypersonic laminar-turbulent transition process in hypervelocity flow were carried out using a 7° half-angle, straight cone with moderate bluntness at zero angle of attack. The tests were conducted at Mach 7.4 in the High Enthalpy Shock Tunnel Göttingen (HEG) of the German Aerospace Center (DLR). Two different nose tips were used resulting in a Reynolds number based on the nose radius of $Re_n \approx 5100$ and $Re_n \approx 10200$. Surface thermocouples, temperature sensitive paint (TSP) and fast-response piezoelectric pressure transducers were used to characterize the transition process. Strong second-mode waves were measured far downstream of the nose tip followed by the appearance of streamwise-oriented streaks of high surface heat flux. Similar streak patterns were observed on flared cones under quiet flow conditions in the Boeing/AFOSR Mach 6 Quiet Tunnel at Purdue University. The present measurement of the primary instability and the spatiotemporal evolution of the streaks represent the first test case reported from a conventional shock tunnel at flight enthalpies and with a highly cooled wall.

1. Introduction

The uncertainty of the boundary layer transition location on a hypersonic vehicle and the corresponding uncertainty in the surface heat flux and skin friction is a major unresolved problem for sustained hypersonic flight. For the design and operation of hypersonic vehicles, reliable transition prediction methods based on a sound understanding of the high-speed boundary layer transition process are required [1]. Since the transition process is largely dependent on the free-stream disturbance level, laminar-turbulent transition in high-speed boundary layers can take different paths, as first outlined by Morkovin [2]. At quiet wind tunnel conditions or in test environments with sufficiently low disturbance levels in the relevant frequency range, the path to turbulence can be described sequentially based on the following specific phenomena. The process is initiated with receptivity in which environmental disturbances couple into the boundary layer. This is followed by the growth of primary instabilities (termed second-mode waves in the present case [3]), the so-called eigenmode growth. After the saturation of the primary instabilities, a region with secondary instabilities exists in which primary and secondary instabilities interact with each other before breaking down to turbulence. This interaction of instabilities has been shown to result in the formation of streamwise-oriented streaks of high skin friction and high heat transfer.

To study the transition process under quiet and noisy test conditions, a large number of experimental studies in the past focused on flared cone geometries, for which detailed analyses were carried out in contrast to straight cone geometries. At the Arnold Engineering Development Center (AEDC), experiments were conducted at Mach 7.93 on the NASA flared cone in Tunnel B, showing an acceleration of the transition process due to the imposed adverse pressure gradient compared to what would have been the case for a straight cone [4,5]. Lachowicz [6,7] conducted experiments under quiet conditions in the NASA Langley Mach 6 Nozzle Test Chamber Facility (M6NTC) showing that the transition process was dominated by second-mode waves. This was confirmed from hypersonic stability experiments on the same NASA flared cone in the same facility with the added feature of wall-temperature regulation to achieve adiabatic and cooled walls [8]. Above a cooled wall (with $T_w < T_0$), larger spatial growth rates were found compared to the adiabatic case (with $T_w \approx T_0$). A direct numerical simulation (DNS) [9] provided consistent results with respect to the aforementioned studies. After the M6NTC was relocated to Texas A&M, the experiments conducted by Lachowicz [6,7] on a flared cone were repeated and the evolution of second-mode waves were studied in more detail [10,11], importantly concluding that their harmonics do not play a role in nonlinear interactions within the boundary layer. The experimental test case on the NASA flared cone in the M6NTC facility was picked up again from a DNS

* Corresponding author.
E-mail address: divek.surujhlal@dlr.de (D. Surujhlal).

https://doi.org/10.1016/j.ast.2025.110846
Received 8 May 2025; Received in revised form 19 August 2025; Accepted 27 August 2025
Available online 4 September 2025

standpoint [12] to study the effect of the cone flare on the nonlinear breakdown process. The DNS revealed the existence of streaks on the cone surface. First experimental observations of streaks resulting from instability interactions were reported by Berridge et al. [13] and Ward et al. [14] on a flared cone under quiet flow conditions using temperature sensitive paint (TSP) in the Boeing/AFOSR Mach 6 Quite Tunnel (BAM6QT) at Purdue University. The authors observed in the streamwise direction the appearance, disappearance and reappearance of streaks under quiet, cold flow conditions only and suspected them to be related to nonlinear interactions of the second-mode waves corresponding to the nonlinear region of the transition process. Importantly, the streaks were classified as 'primary' corresponding to their first appearance and 'secondary' corresponding to their second appearance. Chynoweth et al. [15,16] conducted detailed measurements on the flared cone over a range of unit Reynolds numbers in BAM6QT. For all test cases (without the use of roughness elements in their work), streamwise-growing second-mode waves were measured. Heat transfer measurements with TSP showed the same streak pattern reported by the aforementioned studies [14,17]. An increase of unit Reynolds number caused the streak heating pattern as well as the transition location to move upstream showing that both observations are part of the boundary layer transition process.

The possible breakdown scenarios were extensively explored by Hader and Fasel [18] and Laible et al. [19,20]. In particular, DNS performed for a 7° half-angle straight cone at Mach 3.5 [19,20] showed that the transition process, as initiated by one or multiple pairs of oblique waves, resulted in an 'oblique breakdown' due to their mutual interaction. Furthermore, DNS was carried out of the transition process on a straight and a flared cone at Mach 6 [12]. In this latter case, the transition process was initiated using a primary wave based on linear stability (LST) computations leading to a 'fundamental breakdown' scenario resulting from interaction of the primary instability with oblique modes. By means of DNS, Hader and Fasel [18] found streamwise streaks of very high skin friction and high heat transfer at the cone surface similar to what had been observed in the BAM6QT flared cone experiments. They concluded that fundamental breakdown was a viable transition mechanism for the investigated test case. The streaks were the footprint of an array of counter-rotating vortices, resulting from the interaction of boundary layer instabilities [16].

Hader and Fasel [21] conducted further DNS to investigate the transition process for a sharp 7° half-angle straight cone at Mach 4 using a three-dimensional wave packet to initiate the transition process. The simulation indicated that the aforementioned oblique breakdown was the dominant nonlinear mechanism in that case. In contrast, similar DNS on a sharp 7° half-angle straight cone at Mach 5 revealed that both the fundamental and the oblique breakdown scenarios were possible relevant nonlinear transition mechanisms for the investigated geometry and flow conditions [22]. Furthermore, the wave packet simulations also revealed the possibility of first (oblique) and second-mode interactions. It was additionally shown that the fundamental breakdown, an oblique breakdown and a breakdown initiated by an axisymmetric second-mode with a pair of oblique first mode disturbances were all viable breakdown mechanisms in this case. The breakdown mechanism dominant in a hypervelocity free-stream clearly remains an open topic, which can certainly benefit from experimental measurements within the nonlinear region of a transitional boundary layer.

Over the previous years a number of experimental and numerical studies were conducted in the High Enthalpy Shock Tunnel Göttingen (HEG) of the German Aerospace Center (DLR) to investigate various aspects of the laminar-turbulent transition process in a hypersonic free-stream. Fast-response temperature sensitive paint measurements on a blunted 7° half-angle cone were conducted [23]. The study revealed large-scale unsteadiness in the boundary layer transition onset location and temporally changing streamwise streaks of high heat flux of unknown origin, developing in the transitional region. Experimental studies were carried out investigating second-mode instability growth and breakdown above the same cone model using high-speed schlieren visualization [24]. A quantitative analysis of the second-mode amplitude and its frequency in HEG for the same cone geometry is provided by Marineau et al. [25]. Further to this, transition control was experimentally investigated concerning the effect of transpiration cooling on the second-mode [26] as well as control of the instability waves using acoustically absorptive surfaces [27,28]. In conclusion, the primary instability being a second-mode wave and its role in the transition process on a cone in HEG was investigated in detail.

The present study reports on two test cases using a straight 7° half-angle cone with moderate bluntness in which streamwise-oriented streaks of high surface heat flux were observed for the first time in a conventional, noisy shock tunnel using fast-response temperature-sensitive paint. The corresponding azimuthal wavenumber of the streaks was determined. Furthermore, the development of the second-mode instability was measured along the cone surface upstream of the streak observation, importantly confirming that the second-mode waves are the primary instability and the observed streaks are part of the transition process towards a fully turbulent boundary layer. Although this study alone cannot answer the question of whether fundamental or oblique breakdown dominated the transition process, it serves as a test case in which streaks were observed in a shock tunnel environment for the first time. Complementary DNS conducted by Hader and Fasel [29] based on preliminary studies of results from HEG at the time, confirmed the possibility of a strong fundamental resonance and indicated that secondary waves with a large range of azimuthal wavenumbers can lead to strong resonance. For both test cases presented, the development of 'primary streaks' was repeatably observed.

Table 1
Stagnation conditions for the two test cases resulting in the tabled free-stream conditions in Table 3. Uncertainties are calculated from the standard deviations of the reservoir measurements.

p_0 [MPa]	12.22 ± 0.61
T_0 [K]	2738 ± 8
h_0 [MJ/kg]	3.24 ± 0.01

2. Experimental setup

2.1. The high enthalpy shock tunnel Göttingen (HEG)

Experiments were conducted in the HEG free-piston driven shock tunnel. The unique capability of HEG is the duplication of reentry and hypersonic flight conditions at various altitudes. For this study, these are pertaining to 30 km altitude at Mach 7.4 with moderate enthalpy conditions on the order of 3 MJ/kg. Detailed information on HEG is provided by the DLR [30] including the operational principles of the tunnel, selected geometrical properties of the nozzles, and the conditions in the reservoir and freestream.

The current study details two test cases with similar reservoir and free-stream conditions of the HEG. These are shown in Table 1 for the stagnation properties. Due to the minor stagnation property deviations between the tests (calculated as per Schramm [31]), free-stream parameters are quoted at nominal values (see below). The presented tests were conducted at a wall-to-stagnation temperature ratio $T_w/T_0 \approx 0.1$ with a test time of approximately 3 ms. Information on the free-stream disturbance level in HEG are provided by Wagner et al. [32], which details a measurement campaign coupled with numerical models for frequency-based analyses of freestream disturbances in the HEG.

2.2. HEG free-stream conditions

Free-stream parameters were extracted from a Reynolds-averaged Navier Stokes (RANS) nozzle computation using the experimental

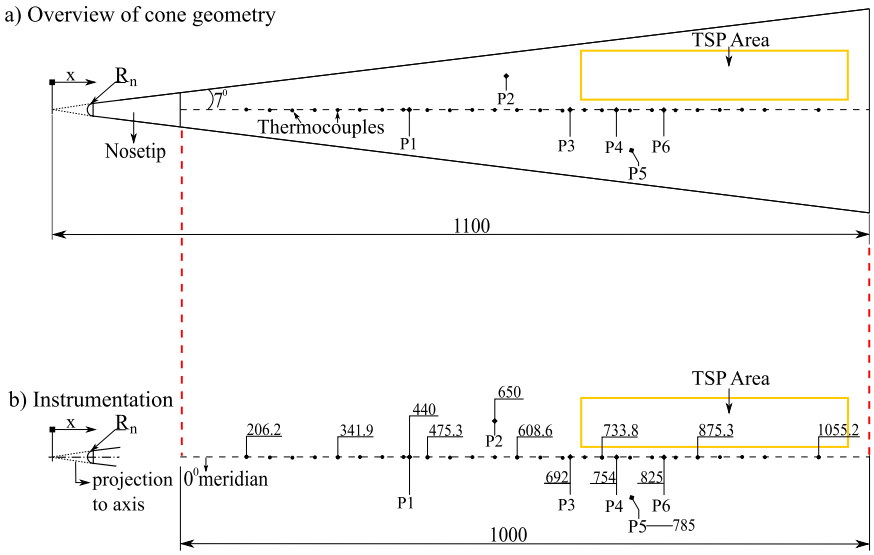

Fig. 1. a) Overview of the cone geometry including transducer labelling for nomenclature; b) Instrumentation layout on the 0° meridian of the cone. The TSP surface is symbolically shown in orange. Sensor ports are indicated by filled circles. Every fifth thermocouple is indicated. PCBs are labelled "P". Dimensions in mm are indicated as streamwise locations downstream of the projected nosetip.

Table 2
Test gas properties and mass fractions (assumed to be constant along the extraction line detailed in Table 3).

Υ_{N_2}	Υ_{O_2}	Υ_{NO}	Υ_O	γ	R[J/kg K]
0.752	0.216	0.032	0.0002	1.3982	288.24

Table 3
HEG free-stream conditions along an extraction line from a RANS computation, method based on [33].

x [m]	z [m]	u[m/s]	v[m/s]	p [Pa]	T[K]	M	$\mu \times 10^5$[Pa. s]	ρ[kg/m^3]
−0.028	0.000	2418.0	0.0	1970.6	302	6.92	1.8566	0.226
0.072	0.033	2420.5	18.1	1831.2	296	7.01	1.8248	0.215
0.171	0.066	2421.1	26.0	1788.2	293	7.04	1.8123	0.212
0.271	0.100	2421.8	30.7	1772.6	292	7.06	1.8074	0.210
0.370	0.133	2420.5	31.3	1791.7	293	7.04	1.8122	0.212

stagnation conditions to enable the numerical rebuilding of the current test cases. Given the minimal variation in stagnation properties between the two cases (see Table 1), a single nozzle case was used to specify the free-stream conditions. An extraction line was defined as per the method used on RANS CFD solutions by Camillo et al. [33]. Table 2 lists the free-stream properties along the extraction line and allows rebuilding the flow field upstream of the investigated straight cone. Species mass fractions are denoted with Υ_i where i denotes the species, γ is the ratio of specific heats and R is the specific gas constant. Along the extraction line, 5 equidistant points were chosen as listed in Table 3, where x and z refer to the streamwise and vertical directions, u and v refer to the streamwise and vertical velocity components, p denotes static pressure, T relates to static temperature, M refers to the Mach number, μ denotes dynamic viscosity, and ρ is the density. When used as anchor points in a spline interpolation, the free-stream conditions can be restored within a variation of 0.1 % of the computed free-stream conditions.

2.3. Test model and instrumentation

The instrumentation layout for the 1100 mm long straight 7° half-angle cone used for these experiments is shown schematically in Fig. 1. Two cases with different nose tip radii (R_n) were examined. *Case 1* is with $R_n = 2.5$ mm and *Case 2* with $R_n = 5$ mm. This gives rise to different entropy layer swallowing lengths x_s, semi-empirically determined following [34] as $x_s = 321$ mm for *Case 1* and $x_s = 813$ mm for *Case 2*.

The model was instrumented with 25 Type E coaxial thermocouples (Medtherm) installed on the 0° meridian. High-speed piezoelectric pressure transducers (PCB 132B38) with a frequency response range from 11 kHz to 1 MHz were additionally used (P1, P3, P4 and P6 on the 0° meridian of the cone in Fig. 1). Transducers P2 and P5 were not placed on the 0° meridian of the cone and are excluded from these analyses.

$$St = \frac{\dot{q}}{\rho_\infty u_\infty c_p (T_0 - T_w)} \tag{1}$$

TSP permitted the field measurement of surface heat flux in the area shown in Fig. 1. The general operating principles of TSP are described by Liu et al. [35], whereas details of the TSP active layer (luminophore and binder) and the application in HEG have been published by Schramm et al. [23,36]. TSP images were captured on a Photron Fastcam SA-Z camera at 100.8 kHz for *Case 1* and 60 kHz for Case 2. The difference in frequency was based on the available resolution limitations of the high-speed camera. A polyethylene terephthalate (PET) adhesive foil was used as the insulating base layer onto which the active layer was applied. This foil was calibrated *in-situ* for the derivation of heat flux $\dot{q}$ [36]. An in-situ calibration was performed using pixels corresponding to an area on the TSP surface and Medtherm coaxial thermocouples located in the immediate vicinity of this area. Heat flux was obtained from the method of Cook and Felderman [37] in which a piecewise temporal integration of the temperature history was defined for calculation of surface heat flux from a thin-film assumption and applied to TSP data. Furthermore, Stanton number was defined based on stagnation temperature and wall temperature [38] (see equation 1), in order to assist formulation of results in non-dimensionalised quantities where the subscript ∞ refers to a free-stream quantity, ρ refers to the density, c_p to the specific heat at constant pressure and u to the velocity in the streamwise direction.

3. Results

3.1. Global observations of boundary layer transition and overview of results

The boundary layer transition information available in this work is depicted in Fig. 2. In Fig. 2a, a sketch of the cone is shown on which transducer locations and the analysed TSP surface are shown.

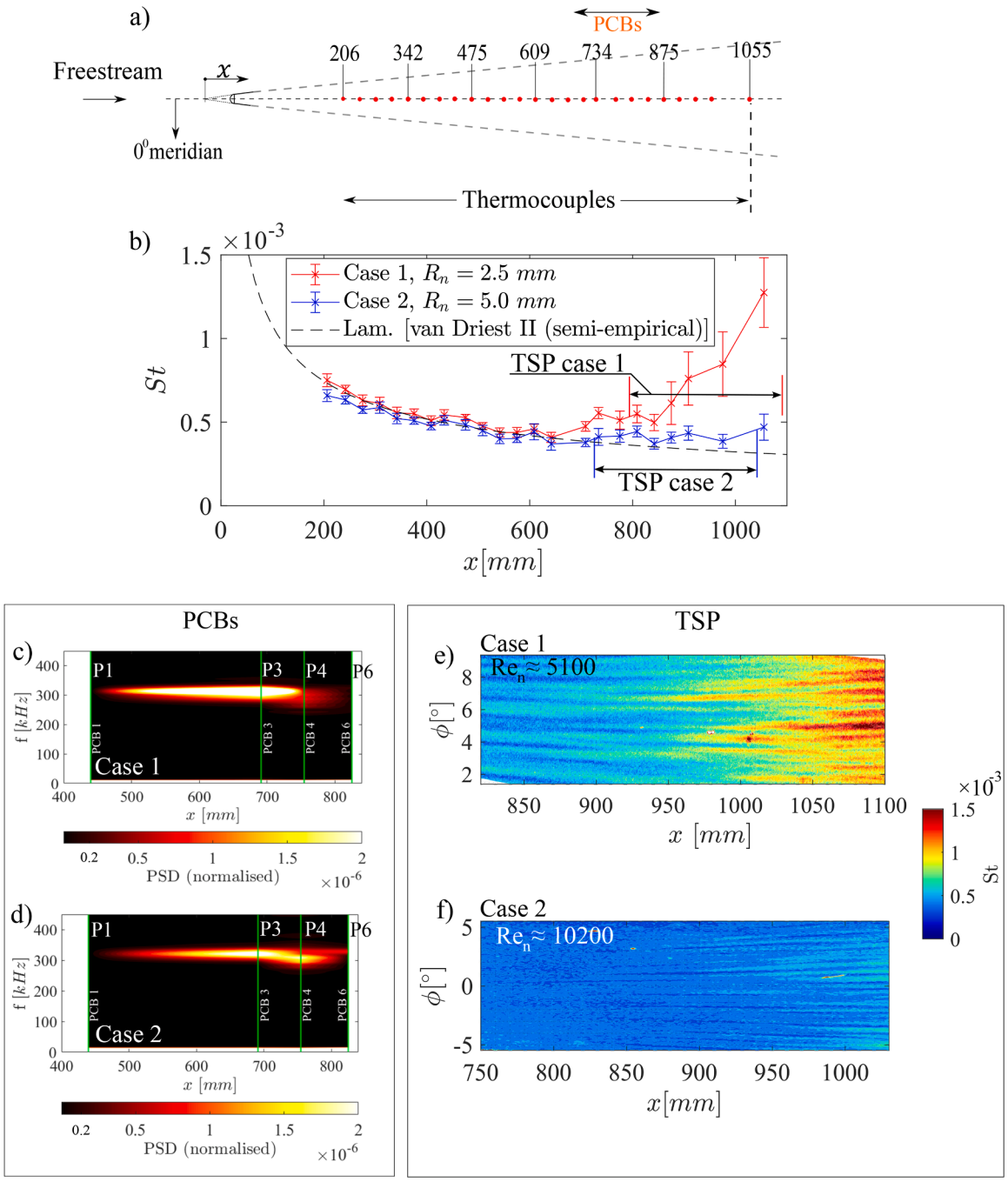

Fig. 2. Summary figure for the information contained in this work. Further analyses refers to these subfigures, with additional information where required. a) Geometric layout of the cone test model including instrumentation locations. b) Time-averaged Stanton number (St) overview of streamwise thermocouple data for Case 1 with $R_n = 2.5$ mm and Case 2 with $R_n = 5$ mm. The reference surface heat flux is given computed from the semi-empirical formulations of van Driest [39]. c), d) PSD of the pressure signals obtained from the fast-response pressure sensors (PCBs) for Case 1 and 2. e), f) Processed TSP results for Case 1 and 2, respectively, from the nonlinear transitional region of the boundary layer depicting streaks of high surface heat flux, observed for the first time in a shock tunnel flow at flight enthalpy.

The time-averaged Stanton number from the thermocouples along the 0° meridian for each case is shown in Fig. 2b. Transition onset occurs further upstream for Case 1 with $R_n = 2.5$ mm than for Case 2 with $R_n = 5.0$ mm which is in line with the work of Softley [40] for the respective Reynolds numbers based on nose radius Re_n.

The spectral information from the fast-response transducers is shown as a contour plot on the bottom left as Fig. 2c and d. A discussion of the measured second-mode instability and its amplification along the streamwise direction is the subject of Section 3.2. The streaks observed on the TSP surface for each case are shown on the top right as Fig. 2e and 2f. The developed TSP images are given for extraction of streak azimuthal wavenumbers, for which a discussion on results obtained deep into the transitional region is the subject of the following subsections.

3.2. Second-mode instabilities

3.2.1. Spectral analysis

The spectral content and amplitudes of the primary instabilities (second-mode waves) for each case were assessed. This was accomplished with the PCBs, located within the transitional region for both

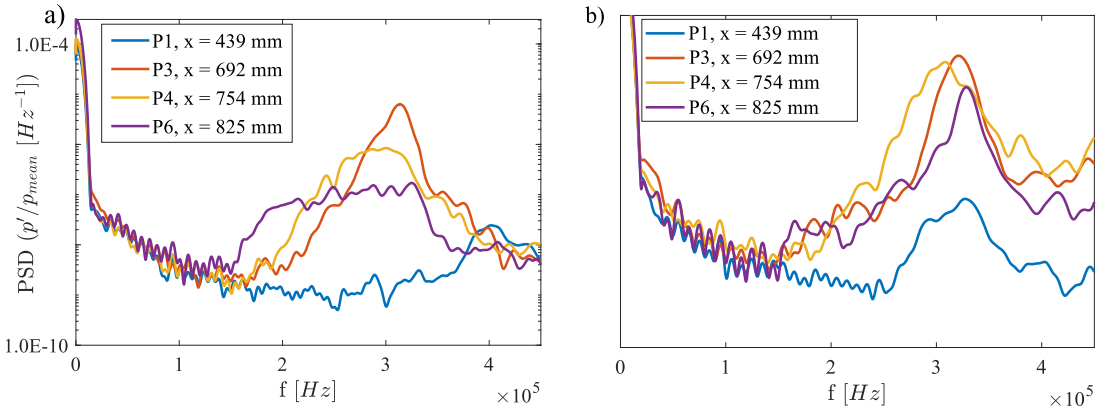

Fig. 3. Frequency-domain analyses for PCB transducers in the vicinity of breakdown. a) Power spectra from PCBs for Case 1. b) Power spectra from PCBs for Case 2.

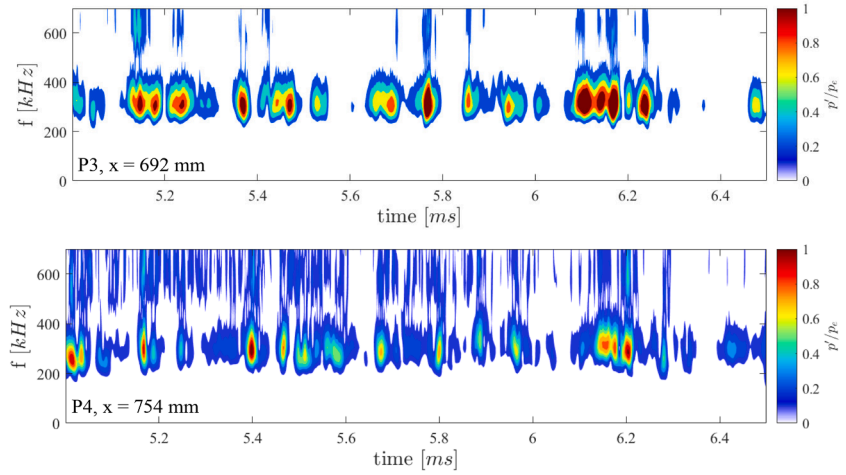

Fig. 4. Time signal of P3 ($x = 692$ mm) and P4 ($x = 754$ mm) for Case 1 displayed in the frequency-time space resulting from a wavelet analysis. Contours are based on pressure perturbations p' normalized by the boundary layer edge pressure p_e.

cases. The PCB power spectral densities (PSDs) for both cases are presented in Fig. 2c and d as a spatial map of PSDs showing the progression of the peaks of the PSD over streamwise distance. Furthermore, the PSDs are also shown in Fig. 3a and b as PSD curves, for Cases 1 and 2, respectively, for more clarity on the individual PSDs. The PSDs were calculated using the method of Welch [41] with Hamming windows and a 25 % overlap. The narrowband peaks of P3 for Case 1 and P3–P6 for Case 2 correspond to second-mode instabilities in the same frequency range as obtained in recent studies in HEG at the same nominal free-stream conditions and model geometry [26].

For Case 1, P3 is just downstream of transition onset, as shown by the surface heat flux data in Fig. 2b. As shown in Fig. 3a, its signal exhibits a narrowband peak at a central frequency of 313 kHz, corresponding with the collated results from Marineau et al. [25] for second modes measured in the HEG at the same freestream conditions and with the same geometry. There are progressively broadening peaks to lower amplitudes at P4 and P6 indicating possible interaction and breakdown of instabilities.

The location of P3 just downstream of transition onset for Case 1 corresponded to second-mode instabilities at their maximum saturated amplitude at this location, as similarly noted in experiments performed by Casper et al. [42]. A wavelet analysis was performed on the P3 signal and normalised with the calculated boundary layer edge static pressure, p_e, based on a laminar CFD analysis. The computational model was solved with the DLR-TAU solver [43,44] considering the nozzle, the model and a part of the test section. The wavelet-transformed signals of P3 and P4 are shown in the frequency-time domain in Fig. 4. For P3, second modes are indicated by the large surface pressure fluctuations located around the 300 kHz range. Simultaneously, there were fluctuations at a higher frequency and lower amplitude centered at around 600 kHz, indicating the presence of an harmonic. The maximum amplitude of the second-mode instabilities was obtained as 28.7 % of p_e at P3. This was calculated by square-rooting the integral of the PSD over designated integral bounds for P3 (Fig. 3a). The integral bounds were the second-mode stopbands f_{band}, defined at −3 dB from the central frequency peak ($f_{band} = [306; 321]$ kHz). This amplitude complements that which was reported by Marineau et al. [25] for the HEG tunnel using a similar test case. Broadening of the second-mode peak is evident for the wavelet-transformed time signal for P4, in addition to the broadening of the higher-frequency harmonics, indicating nonlinear interaction within the boundary layer involving the second-mode instability. Further analysis of the transitional boundary layer in the nonlinear interaction region could be carried out with additional measurements using TSP.

The spectra for Case 2, shown in Fig. 3b, indicated dominant second-mode peaks for P3, P4 and P6 with minimal broadening and an amplitude increase with downstream distance, suggesting that second-mode instabilities were approaching saturation but that interaction and breakdown of instabilities was delayed due to the larger nose radius compared to Case 1. This is also the reason why the peaks in the spectra corresponding to second-mode instabilities are delayed in the streamwise direction for Case 2 compared to those at the same sensor stations for Case 1.

3.3. Observation of streaks in the breakdown region and their analysis

Based on the streamwise location of growth and saturation of the second-modes in the boundary layer, an investigation of the surface heat flux using TSP was carried out in the downstream portion of the cone model. Previous works [16,18] have indicated that this nonlinear region of the transitional boundary layer requires further exploration, but no such investigation was made at flight enthalpies in a shock tunnel under conventional noisy conditions.

The novel result of this TSP investigation is shown in Fig. 2e and f, for Cases 1 and 2, respectively. The graph reports, for the first time, observation of streamwise streaks within the transitional region on the TSP surface in a shock tunnel at representative flight conditions (see Table 3). Here and in the following, ϕ on the vertical axis denotes the cone meridians. There is no coincidence between the range of meridian angles of the two images because the TSP images are taken from different parts of the cone. The appearance of the streamwise streaks on the TSP surface differs for each case, suggesting different stages of breakdown.

3.3.1. Streaks identification from temperature maps

The sequences of temperature snapshots of the cone surface made available by TSP technology enabled us to explore some interesting features exhibited by the flow near the surface itself. Temperature measurements from Case 1 and Case 2 feature a set of streaks of increased temperature running downstream along the meridians. Their running at almost constant ϕ corresponds to a nearly-parallel evolution in the $O(x,\phi)$ reference system shown in Fig. 7. This behavior is well enhanced by the thermal signature of the flow in the spanwise direction. It indicates streaks which, based on DNS analysis [16] for a flare-cone in a quiet tunnel, were suggested to be the thermal traces of an array of counter-rotating vortices resulting from the interaction of boundary layer instabilities. Footprints of this kind of structure were also evidenced by TSP measurements in incompressible conditions [45], but have not yet been observed in high-enthalpy shock tunnels such as the HEG, under flight-representative flow conditions at hypersonic velocity.

3.3.2. Validation of basic features to identify streaks

The maps of the number of validated streaks, $< N(x,t) >$, in Fig. 8b) and g) and their time averages in c) and h) highlight the nearly steady streamwise development of the streaks for Case 1, in contrast to the strongly evolving behavior for Case 2. It is worth noticing the spread of the wavelength around its mean value for Case 1, in contrast to the narrower region occupied by Case 2. In the DNS from Chynoweth et al. [16], streaks formed on the investigated surface as a result of thermal footprints of counter-rotating streamwise vortices. Analogously, the streaks observed in the present experiment were likely the result of the thermal modulation induced by counter-rotating vortices, with the main difference from Chynoweth et al. [16] being the thermal boundary condition at the surface (cold wall in the present experiments in comparison to cold flow in Chynoweth et al. [16]). In fact, a sequence of counter-rotating vortices organizes the flow at the wall as a distribution of thin regions experiencing converging and diverging streamlines because of the interaction between adjacent structures, which push the flow against or expel it from the wall, see Fig. 5. Those manifolds can be topologically classified as sources and sinks, respectively. The resulting thermal signature of the warmer flow over the colder wall can be described as a succession of warmer strips, indicating where the flow hits against the surface, embedded by a pair of colder strips, generated by the convergence of the flow at the surface, before moving away from it.

Based on the expected physical origin of the temperature pattern just described, the procedure of streaks identification has been organized following a sequence of steps that rely on the drawing out and validation of different features, identified at increasing complexity levels. Locations of temperature maxima and minima are validated if each of them belongs to a straight line of temperature maxima and minima peaks developing streamwise. The resulting straight lines are validated if, by observing their succession along the meridians of the cone, they can be grouped three by three in a sequence $T_{\min} - T_{\max} - T_{\min}$, like the one schematized in Fig. 5. The rationale behind this procedure relies on the strong filtering that the three-step sequence applies to the incoming data.

We begin by locating, snapshot by snapshot (at each timestamp t_n) and for each streamwise location, the position of the temperature peaks whose prominence exceeds a fixed threshold. The prominence of a peak measures how much the peak stands out due to its intrinsic height and its location relative to other peaks [46]. A low isolated peak can be more prominent than one that is higher but is an otherwise unremarkable member of a tall range. To make peaks identification less dependent on large-scale temperature variation, a best-fitting (in a least square sense), second-order trend $m(y) = m(x_i, y, t_n)$ is removed from the original temperature profile $T_{i,n}(y) = T(x_i, y, t_n)$. The prominence threshold value is fine-tuned based on the actual distribution of the data peaks within the image.

Since a single maximum is a weak indicator for a streak, the procedure associates temperature peaks found so far with the pair of detectable minima around each of them at the same streamwise position. In this way, the spanwise section of a streak at a certain streamwise position will be characterized by a triplet of points: one temperature peak $T_{\max}$ at ϕ_0 and two minima $T_{\min}$ at ϕ_1 and ϕ_2, where $\phi_1 < \phi_0 < \phi_2$, as schematically sketched in Fig. 5. Fig. 6a reports the maxima and minima of temperature and the identified triplets at a specific streamwise position at time t. Red squares mark the temperature peaks, while the

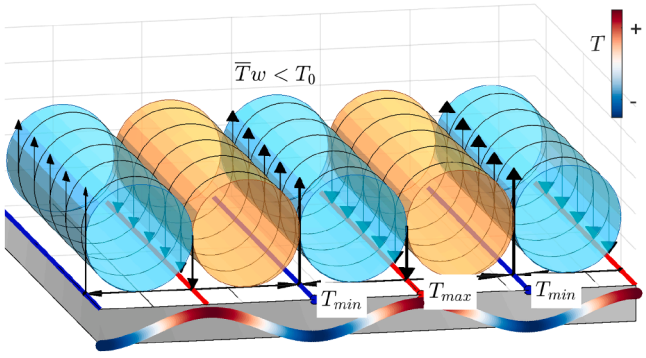

Fig. 5. Idealized sketch of the surface temperature field originated by the interaction between an array of counter-rotating vortices and the surface itself, based on the interpretation of TSP results [45] and DNS [16], with the current case relating to the surface colder than the flow. The succession of flow regions to and from the wall associated with counter-rotating vortex pairs defines a sequence of colder and warmer linear manifolds where $T = T_{\min}$ and $T = T_{\max}$, respectively. Triplets of $T_{\min} - T_{\max} - T_{\min}$ straight lines, composed of temperature peaks, identify the best candidate streaks.

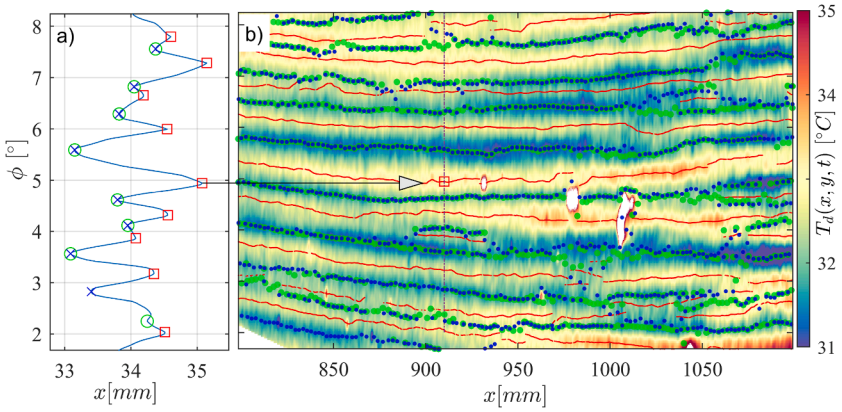

Fig. 6. a) Detail of the section of the temperature map at streamwise location $x = 910$ mm, reporting the spanwise distribution of triplet candidates (one peak with two minima around) time $t = 4.1$ ms (Case 1). Blue crosses and green circles indicate the first lower and upper occurrences of temperature minima around each validated peak, marked by a red square. Validation only checks for the peak's prominence. A non-validated peak can be observed at around $\phi \approx 2.5°$. b) Sequences of triplets validated as streaks after a tracking procedure, overlapped with the corresponding temperature snapshot detail. The streamwise spatial evolution of streaks, including splitting and coalescence, is easily observable. The section at $x = 910$ mm is emphasized, as well as the correspondence of one of the temperature's peaks at $\phi = 5°$. (For interpretation of the references to color in this figure legend, the reader is referred to the web version of this article.)

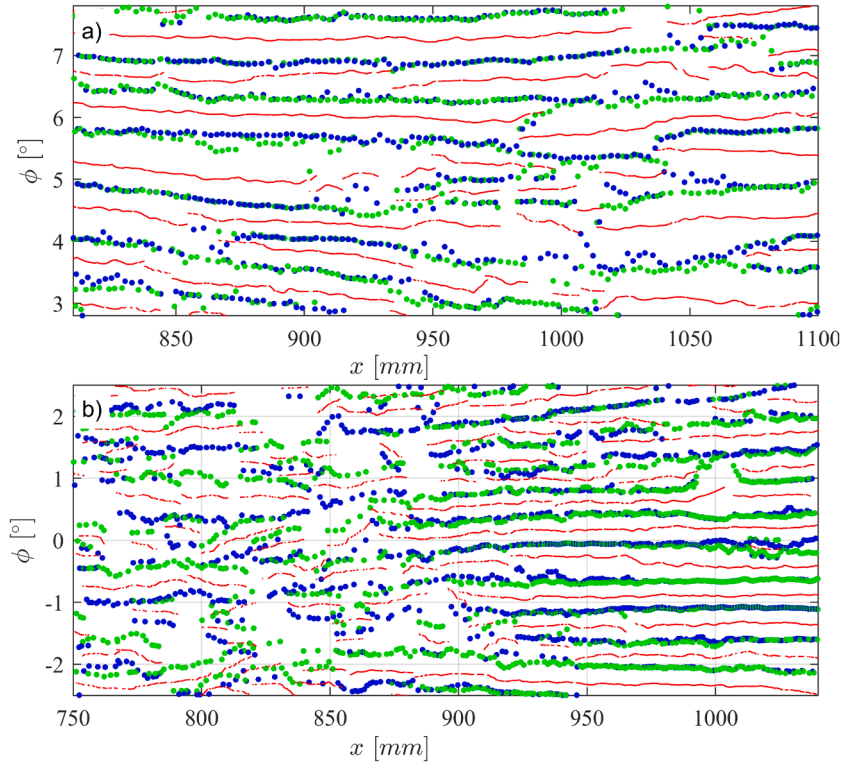

Fig. 7. Validated streaks for Case 1 (a) and Case 2 (b). The homogeneous streamwise streaks evolution of Case 1 is opposed to the sudden change of streak behavior for Case 2. This change occurs at $x \approx 900$ mm. While the streaks' evolution in a) occurs at quite large, almost constant wavelength, their behavior in b) moves from highly irregular to a straight-on arrangement, where the streaks are tightly arranged, exhibiting a shorter wavelength.

minima around them are marked by blue and green dots (for increasing azimuthal values ϕ_1 and ϕ_2). These triplets consist of well-defined sequences of minima and maxima in the temperature profile. They potentially represent streak sections. Due to the flow and measurement complexity, it is not certain that all the triplets defined so far represent the section of a streak. It is necessary to introduce a validation procedure that shifts the attention from the single triplet to the streak intended as a temperature pattern that extends streamwise within the image with certain characteristics.

To confirm or refute each triplet (defined as a locally validated maximum surrounded by two minima) as being the elementary component of a streak, the triplet is tracked against the set of triplets identified all over each image, like in Particle Tracking Velocimetry (PTV) [47]. If it is found that the triplet is part of a sequence propagating downstream, extending for at least a minimum distance, that sequence is validated as a streak. This results in a distinction being made between streaks and spurious features, leading eventually to a more reliable estimation of streak counts.

The tracking is performed on the temperature peak position, and the validated sequences are eventually stored as individual streaks. Outcomes of this procedure are shown in Figs. 6b and 7. In Fig. 6 the temperature peaks and minima in a generic location are placed side-by-side

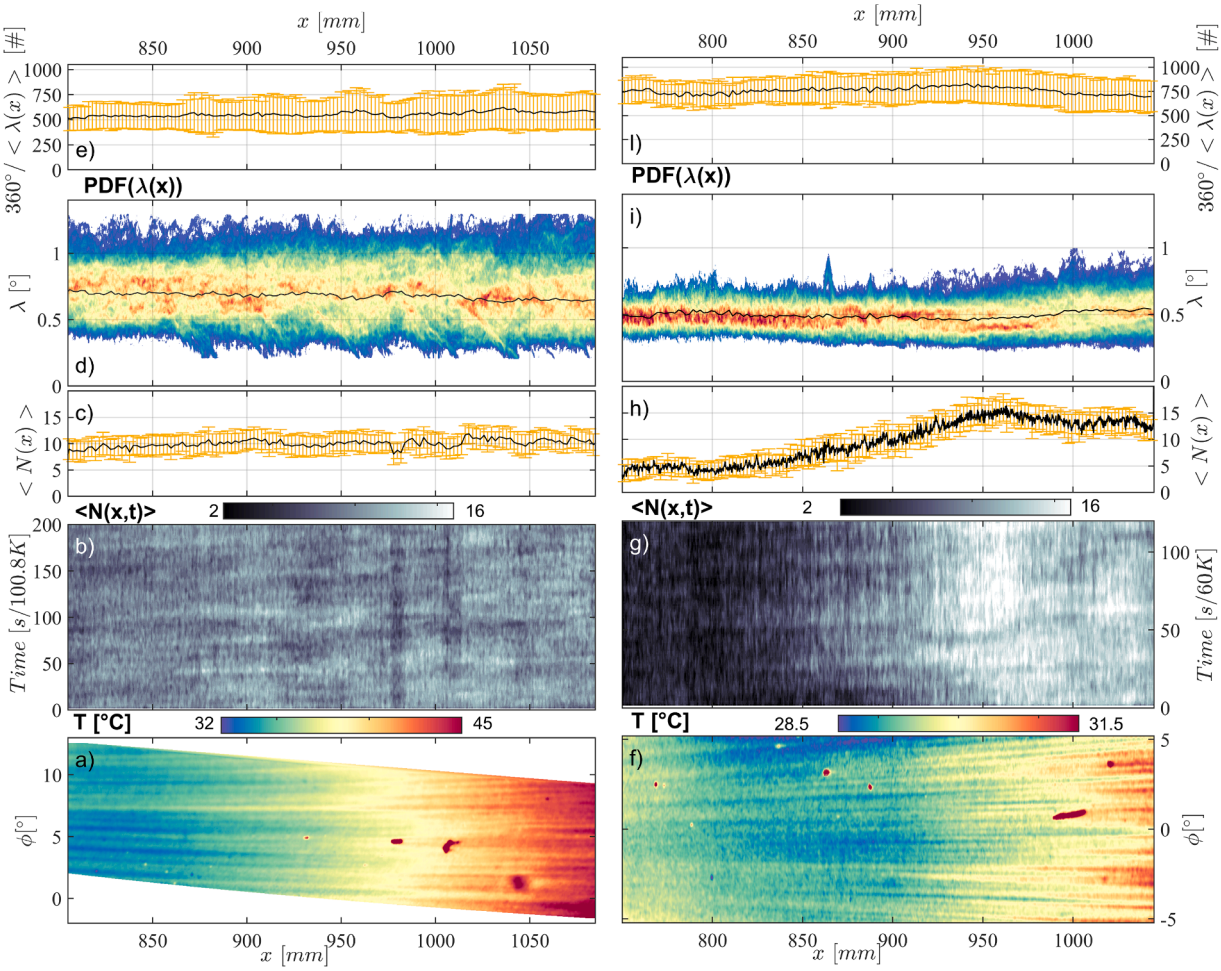

Fig. 8. Experimental streaks statistics for Case 1 (left) and Case 2 (right). Data from the cone wall. a), f) Time-averaged temperature $< T >$ for Cases 1 and 2. b), g) Number of validated streaks $< N(x,t) >$ at each streamwise location x, for each time instant t. c), h) Time average of the number of validated streaks $< N(x) >$ at each streamwise location. The error bar reports the standard deviation of $< N(x) >$ in time. d), i) Distribution of the *PDF* of the streaks' wavelength λ. The black line marks the time-averaged wavelength. e), l) Averaged number of streaks all around the cone circumference, identified as $360°/ < \lambda >$. See Figs. 6 and 7 for a representative sketch of the streaks identification procedure outcome.

with the validated streaks (for Case 1). In most cases, the pair of minimum locations delimiting each streak interferes with the limits of the adjacent streak, and green and blue dots overlap, meaning that the minima on either side of the streaks are coincident, i.e., in that region streaks are saturating their available space.

3.3.3. Statistics of the streaks

Fig. 7(a) and (b) reports a comparison between the streaks extraction for Case 1 and Case 2 at a generic time. The described procedure makes it possible to identify the differences between the streak patterns at first glance. In Case 1, the streaks evolve homogeneously downstream. In contrast, in Case 2 their evolution presents two different stages: in the first part ($x < 900$), they show an irregular and poorly organized behavior, while in the second half, they appear as a highly organized set of streaks, with wavelengths shorter than those of Case 1. This section reports about the statistics of some properties of the streaks, with the aim being to emphasize their case-dependent characters.

The graphs reported in Fig. 8 describe some of the statistics of the streaks as extracted from the temperature maps by TSP. The information in this work only reports statistics obtained on streak distribution in time, each of them as validated within a single temporal snapshot. Application of the procedure to a single image provides information useful to characterize the geometrical characters of the whole set of streaks. Repeating the analysis on the whole time sequence allows observation of the evolution of the same streak over several time steps. The analysis of these dynamics is postponed to future works.

Fig. 8 reports, side by side, several streak-related statistics for Case 1 (left) and Case 2 (right), starting from their time-average (Fig. 8(a) and (f)).

The validation procedure adopted for the streaks does not guarantee the space to be filled by the streaks themselves. The process of instability breakdown flattens the temperature distribution in flow regions where it is still ongoing, and smears the presence of streaks, if any. From this point of view, the number of validated streaks for each streamwise location in Fig. 8(b) and (g) also provide information on the state of the flow. These graphs compare the spanwise-averaged number of validated streaks $< N(x,t) >$, at each streamwise location and for each time t. In addition, Fig. 8(c) and (h) report the time-average $< N(x) >$ and the standard deviation of such distributions. It is evident that there is an almost steady evolution of the validated streaks $< N(x) >$ for Case 1, compared to its streamwise increase for Case 2.

The mean values of $\lambda(x)$ obtained by the streak analysis (black, narrow lines in Fig. 8d) and i))) are then used to estimate the corresponding distribution of the total number of streaks around the cone over the stream location.

This is estimated to be $k_c \approx 580$ streaks for Case 1 and $k_c \approx 620$ for Case 2, based on the downstream portion of the domain, where

the streaks deliver the strongest signal. Complementary highly resolved DNS [29] using approximated HEG test conditions confirmed that large linear amplification of second-mode instabilities combined with fundamental resonance breakdown mechanisms corresponded to streak counts in the range reported here. It is worth noticing that the spreading of the estimated number of streaks around its mean value is larger for Case 1 than for Case 2. Notwithstanding the almost steady evolution of its mean value, the *PDF* of λ for Case 1 exhibits a wider standard deviation than for Case 2 (Fig. 8(d) and (i)), which reflects the wider variability of the total number of streaks (Fig. 8(e) and (l)). The distribution of the wavelength probability density function ($PDF(\lambda(x))$) of the validated streaks is sketched in Fig. 8(d) and (i), where each column reports the occurrence probability of λ. Again, a comparison shows for Case 1 a steady-state wavelength evolution along a broad band around the mean value, while Case 2 reports an increasing wavelength along the streamwise direction x, following a narrower band around the mean value.

4. Conclusions

This work analyses the breakdown process of second-mode instabilities on a straight cone with a moderate nose bluntness of $R_n = 2.5\,\text{mm}$ (Case 1) and $R_n = 5\,\text{mm}$ (Case 2) resulting in Reynolds numbers based on the nose radius of $Re_n \approx 5100$ and $Re_n \approx 10200$. Experiments were conducted at HEG at a free-stream Mach number of $M = 7.4$ and stagnation enthalpies of $h_0 \approx 3\ MJ/kg$. Measured primary instabilities (second-mode waves) showed significant spectral broadening for Case 1 indicating nonlinear interaction of these instabilities within the boundary layer. The maximum second-mode amplitude was estimated to be 28.7 % of the boundary layer edge pressure for this case. As a result of increased nose bluntness, Case 2 displayed sustained second-mode instabilities in a narrow spectral bandwidth associated with a transition onset further downstream than for Case 1. Within the transitional region of the boundary layer, streamwise-oriented streaks were observed and examined for the first time in a shock tunnel under conventional noisy, flight enthalpy, free-stream conditions; this was made possible for both cases using TSP. For Case 1, whilst the streaks are more prominent due to the transition of the boundary layer being further along in its development, there is a large spread of wavelengths detected by a robust streak detection methodology. This indicates streaks of multiple spanwise wavelengths present at different streamwise locations, suggesting bifurcations and splitting of the streaks, especially in the downstream direction as turbulence is approached. For Case 2, there is a markedly narrower band of streak wavelengths, allowing to estimate the spanwise wavelength of the streaks with higher confidence. In this case, broadening of the streaks was evident towards the downstream end of the TSP region. This study of the streaks in the nonlinear transitional region of the boundary layer and specification of free-stream flow conditions serves as the first test case for numerical modeling of secondary instability breakdown and boundary layer transition on blunted cones at flight enthalpy levels, highly cooled walls and conventional (noisy) test conditions.

CRediT authorship contribution statement

Divek Surujhlal: Writing – review & editing, Writing – original draft, Investigation, Formal analysis; **Alexander Wagner:** Writing – review & editing, Supervision, Investigation, Conceptualization; **Marco Costantini:** Writing – review & editing, Supervision, Investigation; **Massimo Miozzi:** Writing – review & editing, Writing – original draft, Investigation, Formal analysis, Data curation.

Data availability

Data can be made available upon reasonable request.

Declaration of competing interest

The authors declare that they have no known competing financial interests or personal relationships that could have appeared to influence the work reported in this paper.

Funding

This work was supported by AFOSR grant FA9550-16-1-0456 and the German Aerospace Center (DLR).

References

[1] S. Karl, T. Bykerk, Sustainable space technologies—strategies toward a predictive aerothermal design of re-useable space transportation systems, Rev. Sci. Instrum. 95 (2) (2024). https://doi.org/10.1063/5.0177075
[2] M.V. Morkovin, Critical evaluation of transition from laminar to turbulent shear layers with emphasis on hypersonically travelling bodies, Technical Report AFFDL-TR-68-149, Air Force Flight Dynamics Laboratory, 1969.
[3] L.M. Mack, Linear stability theory and the problem of supersonic boundary-layer transition, AIAA J. 13 (1975) 278–289.
[4] R.L. Kimmel, The effect of pressure gradients on transition zone length in hypersonic boundary layers, Flight Dynamics Directorate, Wright Laboratory, Air Force Materiel Command, 1993.
[5] R.L. Kimmel, J. Poggie, Effect of total temperature on boundary-layer stability at Mach 6, AIAA J. 38 (9) (2000) 1754–1755.
[6] J.T. Lachowicz, N. Chokani, S.P. Wilkinson, Boundary-layer stability measurements in a hypersonic quiet tunnel, AIAA J. 34 (12) (1996) 2496–2500. https://doi.org/10.2514/3.13430
[7] J.T. Lachowicz, N. Chokani, S.P. Wilkinson, Hypersonic boundary layer stability over a flared cone in a quiet tunnel, AIAA, 1996. AIAA 1996-0782.
[8] A.E. Blanchard, G.V. Selby, S.P. Wilkinson, A quiet tunnel investigation of hypersonic boundary-layer stability over a cooled, flared cone, Tech. Rep., NASA, 1996. NASA-CR-202200.
[9] C.D. Pruett, C.L. Chang, Direct numerical simulation of hypersonic boundary-layer flow on a flared cone, Theor. Comput. Fluid Dyn. 11 (1) (1998) 49–67. https://doi.org/10.1007/s001620050080
[10] J. Hofferth, W. Saric, Boundary-layer transition on a flared cone in the Texas A&M Mach 6 quiet tunnel, AIAA, 2012. AIAA 2012-0923, https://arc.aiaa.org/doi/abs/10.2514/6.2012-923.
[11] J.W. Hofferth, R.A. Humble, D.C. Floryan, W.S. Saric, High-bandwidth optical measurements of the second-mode instabilityin a Mach 6 quiet tunnel, AIAA, 2013. AIAA 2013-0378.
[12] A. Laible, H. Fasel, Numerical investigation of hypersonic transition for a flared and a straight cone at Mach 6, AIAA, 2011. AIAA 2011–3565.
[13] D.C. Berridge, A. Chou, C.A.C. Ward, L.E. Steen, P.L. Gilbert, T.J. Juliano, S.P. Schneider, J.E. Gronvall, Hypersonic boundary-layer transition experiments in a Mach-6 quiet tunnel, 2010. AIAA 2010-1061.
[14] C. Ward, B. Wheaton, A. Chou, D. Berridge, L. Letterman, R. Luersen, S. Schneider, Hypersonic boundary-layer transition experiments in the boeing/AFOSR Mach-6 quiet tunnel, AIAA, 2012. AIAA 2012-0282. https://doi.org/10.2514/6.2012-282
[15] B.C. Chynoweth, Measurements of Transition Dominated by the Second-Mode Instability at Mach 6, Ph.D. thesis, Purdue University, 2018.
[16] B.C. Chynoweth, S.P. Schneider, C. Hader, H. Fasel, A. Batista, J. Kuehl, T.J. Juliano, B.M. Wheaton, History and progress of boundary-layer transition on a Mach-6 flared cone, J. Spacecr. Rockets 56 (2) (2019) 333–346. https://doi.org/10.2514/1.a34285
[17] D.C. Berridge, K.M. Casper, S.J. Rufer, C.R. Alba, D.R. Lewis, S.J. Beresh, S.P. Schneider, Measurements and computations of second-mode instability waves in three hypersonic wind tunnels, AIAA, 2010. AIAA 2010–5002.
[18] C. Hader, H.F. Fasel, Direct numerical simulations of hypersonic boundary-layer transition for a flared cone: fundamental breakdown, J. Fluid Mech. 869 (2019) 341–384. https://doi.org/10.1017/jfm.2019.202
[19] A. Laible, C. Mayer, H.F. Fasel, Numerical investigation of transition for a cone at Mach 3.5: oblique breakdown, AIAA, 2009. AIAA 2009–3557.
[20] A. Laible, H. Fasel, Temporal direct numerical simulations of oblique breakdown for a cone at Mach 3.5, AIAA, 2011. AIAA 2011-209.
[21] C. Hader, H.F. Fasel, Direct numerical simulations of hypersonic boundary-layer transition for a straight cone at Mach 4: oblique breakdown, AIAA, 2021. AIAA 2021–2863.
[22] C. Hader, N. Deng, H.F. Fasel, Direct numerical simulations of hypersonic boundary-layer transition for a straight cone at Mach 5, AIAA, 2021. AIAA 2021-0743.
[23] H. Ozawa, S.J. Laurence, J.M. Schramm, A. Wagner, K. Hannemann, Fast response temperature sensitive paint measurements on a hypersonic transition cone, Exp. Fluids 56 (1853) (2014). https://doi.org/10.1007/s00348-014-1853-y
[24] S.J. Laurence, A. Wagner, K. Hannemann, Experimental study of second-mode instability growth and breakdown in a hypersonic boundary layer using high-speed schlieren visualization, J. Fluid Mech. 797 (2016) 471–503. https://doi.org/10.1017/jfm.2016.280
[25] E.C. Marineau, G. Grossir, A. Wagner, M. Leinemann, R. Radespiel, H. Tanno, T.P. Wadhams, B.C. Chynoweth, S.P. Schneider, R. Wagnild, K.M. Casper, Compilation and analysis of second mode amplitudes on sharp cones in hypersonic wind tunnels, AIAA, 2018. AIAA 2018-0349, https://doi.org/10.2514/6.2018-0349

[26] G.P. Camillo, A. Wagner, C. Dittert, L. Benjamin, V. Wartemann, J. Neumann, R. Hink, Experimental investigation of the effect of transpiration cooling on second mode instabilities in a hypersonic boundary layer, Exp. Fluids 61 (162) (2020) 1–19.
[27] A. Wagner, K. Hannemann, M. Kuhn, Ultrasonic absorption characteristics of porous carbon-carbon ceramics with random microstructure for passive hypersonic boundary layer transition control, Exp. Fluids 55 (6) (2014). https://doi.org/10.1007/s00348-014-1750-4
[28] V. Wartemann, A. Wagner, D. Surujhlal, C. Dittert, OCTRA as ultrasonically absorptive thermal protection material for hypersonic transition suppression, CEAS Space J. 15 (2023) 959–969.
[29] C. Hader, H.F. Fasel, Direct numerical simulations of hypersonic boundary-layer transition for a straight cone at Mach 7, AIAA, 2021. AIAA 2021–2865.
[30] Deutsches Zentrum für Luft - und Raumfahrt (DLR), The high enthalpy shock tunnel Göttingen of the german aerospace center (DLR), J. Large-Scale Res. Facil. 4 (2018) A133. http://dx.doi.org/10.17815/jlsrf-4-168
[31] J.M. Schramm, Aerothermodynamische Untersuchung einer Wiedereintrittskonfiguration und ihrer Komponenten in einem impulsbetriebenen Hochenthalpie-Stoßkanal, Ph.D. thesis, Georg-August-Universität Göttingen, 2008.
[32] A. Wagner, E. Schülein, R. Petervari, K. Hannemann, S.R.C. Ali, A. Cerminara, N.D. Sandham, Combined free-stream disturbance measurements and receptivity studies in hypersonic wind tunnels by means of a slender wedge probe and direct numerical simulation, J. Fluid Mech. 842 (2018) 495–531. https://doi.org/10.1017/jfm.2018.132
[33] G.P. Camillo, A. Wagner, T. Toki, C. Scalo, Combined experimental and numerical investigation of a hypersonic turbulent boundary layer by means of FLDI and large-eddy simulations, Aerospace 10 (6) (2023) 570–601. https://doi.org/10.3390/aerospace10060570
[34] N.R. Rotta, Effects of Nose Bluntness on the Boundary Layer Characteristics of Conical Bodies at Hypersonic Speeds, Technical report AD0645668, New York University, Department of Aeronautics and Astronautics, 1966.
[35] T. Liu, J.P. Sullivan, K. Asai, C. Klein, Y. Egami, Pressure and Temperature Sensitive Paints, Springer International Publishing, 2021. https://doi.org/10.1007/978-3-030-68056-5
[36] J.M. Schramm, K. Hannemann, H. Ozawa, W. Beck, C. Klein, Development of temperature sensitive paints in the high enthalpy shock tunnel Göttingen, HEG, in: 8th European Symposium on Aerothermodynamics for Space Vehicles, 2015.
[37] J.C. Cook, E.J. Felderman, Reduction of data from thin-film heat-transfer gages—A concise numerical technique, AIAA J. 4 (1966) 561–562. https://doi.org/10.2514/3.3486
[38] H.T. Nagamatsu, W.T. Petit, R. Sheer, Heat transfer on a flat plate in continuum to rarefied hypersonic flows at Mach numbers of 19.2 and 25.4. NASA contractor report. 1970.
[39] E.R. van Driest, The problem of aerodynamic heating, in: Aeronautical Engineering Review, 1956, pp. 26–41.
[40] E.J. Softley, Boundary layer transition on hypersonic blunt, slender cones, AIAA, 1969. AIAA 69–705, http://dx.doi.org/10.2514/6.1969-705.
[41] P. Welch, The use of fast Fourier transform for the estimation of power spectra: a method based on time averaging over short, modified periodograms, IEEE Trans. Audio Electroacoust. 15 (2) (1967) 70–73.
[42] K.M. Casper, S.J. Beresh, R.M. Wagnild, J.F. Henfling, R.W. Spillers, B.O.M. Pruett, Simultaneous pressure measurements and high-speed schlieren imaging of disturbances in a transitional hypersonic boundary layer, AIAA, 2013. AIAA 2013–2739.
[43] B. Reimann, V. Hannemann, Numerical investigation of double-cone and cylinder experiments in high enthalpy flows using the DLR TAU code, AIAA, 2010. AIAA 2010-1282.
[44] A. Mack, V. Hannemann, Validation of the unstructured DLR-TAU-code for hypersonic flows, AIAA, 2002. AIAA 2002–3111.
[45] M. Miozzi, A. Capone, F. Di Felice, C. Klein, T. Liu, Global and local skin friction diagnostics from TSP surface patterns on an underwater cylinder in crossflow, Phys. Fluids 28 (12) (2016) 1–23. https://doi.org/10.1063/1.4968525
[46] The MathWorks, Inc., Signal Processing Toolbox, Natick, Massachusetts, United States, 2024b edition, 2014. https://www.mathworks.com/help/signal/.
[47] M. Miozzi, G. Querzoli, PTV and POD analysis of the instabilities in a quasi two-dimensional convective flow, Appl. Sci. Res. 56 (2–3) (1996). https://doi.org/10.1007/bf02249383